Sub-Pixel SAR Image Registration through Parabolic Interpolation of the 2D Cross-Correlation

Luca Pallotta, *Senior Member, IEEE*, Gaetano Giunta, *Senior Member, IEEE*, and Carmine Clemente, *Senior Member, IEEE*

***Abstract*—In this paper the problem of Synthetic Aperture Radar (SAR) images coregistration is considered. In particular, a novel algorithm aimed at achieving a fine sub-pixel coregistration accuracy is developed. The procedure is based on the parabolic interpolation of the 2D cross-correlation computed between the two SAR images to be aligned. More precisely, from the Two-Dimensional (2D) cross-correlation, a neighborhood of its peak value is extracted and the interpolation of both the 2D paraboloid and the two alternative 1D parabolas are computed to provide the finer misregistration estimation with a sub-pixel accuracy. The main advantage of the proposed framework is that the overall computational burden is only due to the 2D cross-correlation estimation since the parabolic interpolation is calculated with a closed-form expression. The results obtained on real recorded Unmanned Aerial Vehicle (UAV) SAR data highlight the effectiveness of the proposed approach as well as its capabilities to provide some benefits with respect to other available strategy.**

***Keywords*—Synthetic Aperture Radar, SAR coregistration, 2D cross-correlation, parabolic interpolation, sub-pixel coregistration, UAV SAR.**

I. Introduction

Synthetic Aperture Radar (SAR) processing and applications have seen a severe growth during the last decades. This is mainly due to the advances in the signal processing techniques but also on the utilized platform (viz. satellite, aerial, Unmanned Aerial Vehicle (UAV), missile) that have laid the foundations for the development of increasingly sophisticated and performing algorithms. In this regard, a fundamental step that needs particular attention in its implementation as well as an ever greater accuracy is the coregistration. As a matter of fact, the availability of two or more registered images is on the basis of several fundamental SAR applications, such as interferometry, differential interferometry, change detection, environmental monitoring, polarimetry, and so on.

Coregistration of a couple or a series of images consists in aligning one or more images (referenced to as slave) with respect the first one (referred to as master) so that corresponding pixels in the two images should refer to the same objects or scatterers in the observed scene [1]–[3]. In general, this alignment process takes place by calculating one or more tie points on the master image and then searching for them in the slave. These points give the amount of the misalignment between the two images; therefore, a proper shift, in both range and azimuth directions, followed by a specific resample is then applied on the slave image. Of course, several strategies can be applied in performing the above mentioned alignment, for instance a global shift can be applied to the entire imagery and/or considering different range and azimuth shifts for different patches extracted over them. One strategy could consist in utilizing the Two-Dimensional (2D) cross-correlation between the master and slave image to identify the extent of the displacement, however, the increasing demands of modern SAR applications in terms of coregistration accuracy have led over the years to the diffusion of registration algorithms with subpixel accuracy.

The importance and usefulness of coregistration in the SAR context is demonstrated by the number of works and algorithms that have been disseminated in the open Literature over the years. As a matter of fact, some works have considered the exploration of the cross-correlation between master and slave for registration purposes, such as in [4], [5] where the cross-correlation peak is first determined to produce coarse registered images. The finer registration is then obtained in the former exploiting some texture features whereas in the latter thanks to interpolations of blocks within the image itself. In addition, [6], exploiting some shift properties of the Fourier transform, derives the cross-correlation between the two SAR images to register in the spectral domain in a computational efficient manner. Again, in [7], [8] a nonlinear optimization problem that maximizes the coherent cross-correlation of the two images is derived such that to overcome the problem of images oversampling and offset searching problem. In fact, in [9] the misregistration between two SAR images is estimated thanks to the exploitation of their spectral characteristics; however this approach does not consider any kind of interpolation but utilizes the phase information extracted by different looks in the spectral domain. Moreover, [10] proposes a new framework for robust and accurate image registration that utilizes the mutual information as a measure of similarity especially in non-Gaussian environments and that exploits the diffusion to properly model the displacement field. In [11], the authors design a methodology for the regularization of the displacement vector field based on two steps, where firstly a threshold is applied to remove possible outliers and then the inpainting technique is utilized so as to fill in the gaps left by the previous process. Another interesting approach is the one followed in [12], that resorts to a geometrical approach and tries to obtain an accurate registration of multitemporal and

L. Pallotta and G. Giunta are with the Department of Engineering, University of Roma Tre, via Vito Volterra 62, 00146 Rome, Italy (e-mail: luca.pallotta@uniroma3.it, gaetano.giunta@uniroma3.it).

C. Clemente is with the Department of Electronic and Electrical Engineering, University of Strathclyde, G1 1XW Glasgow, Scotland (e-mail: carmine.clemente@strath.ac.uk).

multibaseline images exploiting additional information, viz. orbital information and an available Digital Elevation Model (DEM). Reference [13] gives a procedure aimed at evaluating the optimum tie point interval for SAR coregistration that exploits a wavelet transformation to obtain a proper autocorrelation coefficient decomposition of the SAR images. Another example can be found in [14], where the authors study the problem of coregistration for Sentinel-1 Terrain Observation by Progressive Scans (TOPS) time-series image in regions characterized by a low coherence.

Some alternatives to the classic approaches can be found in [15]–[20], where some novel feature-based methods are developed for co-registration purposes for their low computational time. In particular, [15] proposes a feature-based approach that is based on features detection after image segmentation obtained through a level set strategy. In [16] a robust and efficient method for SAR image registration is provided; it jointly exploits image segmentation, scale invariant feature transform (SIFT) and outlier removal. Analogously, [19] devises a procedure for SAR image coregistration that exploits the phase congruency and also enforce some spatial constraints. Precisely, from the phase congruency images some features are extracted by means of the so called SIFT operator. Moreover, the enforced spatial constraints on the detected points is also considered so as to increase the number of correctly assigned correspondences. In [17], a SAR image registration algorithm is designed exploring rotation-invariant features based on a polar transformation of the local regions. Furthermore, in [18] the authors provide a local matching algorithm which extracts some texture features from the SAR images and then properly matches them through a minimum distance criterion. Also, in [20] exploiting the SIFT method, a framework to obtaining accurate coregistration of oblique SAR images is devised. Further readings could be also [21], [22]. Finally, some other interesting works concerning the coregistration of multimodal images (e.g., SAR and optical) are [23]–[26].

To the authors' best knowledge no work already presented in the literature realizes an interpolation of the 2D cross-correlation between the SAR image couple to refine the coarse estimate associated with its peak value. In fact, a typical approach to move towards a subpixel resolution consists in oversampling the original images with a consequent increment in the overall computational burden for the system at hand. Therefore, to overcome this limitation, in this paper we propose a novel low-computational cost framework for SAR image coregistration with a subpixel accuracy based on the parabolic interpolation of the 2D cross-correlation. Precisely, we extract from the 2D cross-correlation a neighborhood of its maximum value and, according to the lead of [27], we estimate the vertex position (viz. its range and azimuth) of the interpolating paraboloid passing through the points in it contained. Precisely, we exploit the results of [27] where the paraboloid interpolation was introduced with the aim of providing a block-oriented motion estimation in video sequences to refine, at a sub-pixel level, the amount of displacement described by the cross-correlation peak location. More specifically, the proposed coregistration framework comprises two different alternatives, viz. in one case the paraboloid vertex position is directly estimated in the 2D domain with the aims of six pixels in the neighborhood, and a second case that estimates the vertex position of the two alternating One-Dimensional (1D) cuts of the 2D cross-correlation from five of the extracted pixels. Since both the 2D paraboloid and the two 1D parabolas vertices positions are closed-form computed, the overall computational burden is only dictated by the 2D cross-correlation evaluation stage. At the analysis stage, some study cases are illustrated to assess the capability of the proposed algorithm to improve the coregistration accuracy in different situations of practical interest. In particular, the analyses are conducted on the Ku-band spotlight UAV SAR images collected by a Sandia National Laboratory test platform, utilizing as figure of merit the absolute estimation error of the unknown displacement and coherence magnitude of the quoted registered couple. The results demonstrate the effectiveness of the proposed approach in providing a fine images coregistration and show that some advantages with respect to other counterparts can also be observed.

The paper is organized as follows. Section II formulates the problem, providing the theory of the parabolic interpolation of a 2D ambiguity function together with the description of the proposed algorithm for SAR images coregistration. Section III illustrates some classic coregistration strategies that are then utilized as comparison for the analyses reported in Section IV. The results demonstrate the benefits of the proposed method in terms of sub-pixel coregistration on SAR images acquired by a UAV both for single-look and multi-look images. Finally, Section V concludes the paper and outlines some possible future research tracks.

NOTATION

We adopt the notation of using boldface for vectors $\boldsymbol{a}$ (lower case), and matrices $\boldsymbol{A}$ (upper case). The kth entry of $\boldsymbol{a}$ is denoted by $\boldsymbol{a}(k)$, and the (k,n)-th entry of $\boldsymbol{A}$ is denoted by $\boldsymbol{A}(k,n)$. As to numerical sets, $\mathbb{C}$ is the set of complex numbers, and $\mathbb{C}^{K\times N}$ is the Euclidean space of $(K \times N)$-dimensional complex matrices (or vectors if $N = 1$). The conjugate operator is denoted by the symbol $(\cdot)^*$, while $|\cdot|$, and $(\cdot)^*$ indicate the modulus and complex conjugate of the argument, respectively. The symbol $\mathcal{F}(\cdot)$ represents the Fourier transform of the argument, whereas $\mathbb{E}[\cdot]$ stands for statistical expectation. The letter j indicates the imaginary unit, i.e., $j = \sqrt{-1}$. Finally, $*$ denotes the convolution operator whose result is selected only for the valid values.

II. COREGISTRATION BASED ON PARABOLIC INTERPOLATION

This section describes the proposed algorithm for sub-pixel image coregistration of two SAR images representative of the same observed scene. Precisely, the procedure is based on the parabolic interpolation, introduced in [27] with the aim of providing a block-oriented motion estimation in video sequences, of the 2D cross-correlation between the quoted images. This kind of approach allows to obtain an estimation of the image displacement with a sub-pixel accuracy and at the

same time keeping almost unaffected the overall computational burden. In the next subsections, the theory defining the 2D and 1D parabolic interpolation for a 2D ambiguity function is first introduced, then the novel sub-pixel coregistration algorithm is described in details. Finally, the last subsection provides a quick description of some existing algorithm for SAR image registration that will be compared in the analyses section with the proposed one.

A. Paraboloid Interpolation of the 2D Ambiguity Function

Let us consider a 2D ambiguity function, referred to in the following as $\boldsymbol{A}(x,y)$, and let assume that a set of its values is somehow available, say $\boldsymbol{A}(x_i,y_l)$, $i = I_1,\ldots,I_2$, $l = L_1,\ldots,L_2$, with (x_i,y_l) defining a discrete set. Typically, the maximum (or minimum) value of the ambiguity $\boldsymbol{A}(x_i,y_l)$ differs from that of the continuous valued counterpart, due to the discretization process, noise, and so on. A way to properly identify the true maximum position of a 2D ambiguity function could consist in interpolating it over the 2D discretized grid. Specifically, when such a situation arises, the available samples of the ambiguity function can be exploited to obtain a finer estimate of the maximum. A simple way to perform this function consists in examine this problem as a joint accurate estimation of the two parameters of the ambiguity function, viz. x and y, [27]. The starting point is a preliminary estimate of the actual coarse maximum, say $\boldsymbol{A}(x_0,y_0)$, located in (x_0,y_0), of the measured ambiguity samples $\boldsymbol{A}(x_i,y_l)$, $i = I_1,\ldots,I_2$, $l = L_1,\ldots,L_2$. Now, if the expected ambiguity function $\mathbb{E}\left[\boldsymbol{A}(x,y)\right]$ is well approximated in the neighborhood of its maximum by a 2D paraboloid, the fine estimator searches for the apex of such parabolic function, whose six coefficients are determined from six values of the estimated ambiguity function taken around the coarse maximum [27], namely

$$\begin{cases} a_1 = \boldsymbol{A}(x_0,y_0) \\ a_2 = \boldsymbol{A}(x_1,y_0) \\ a_3 = \boldsymbol{A}(x_{-1},y_0) \\ a_4 = \boldsymbol{A}(x_0,y_1) \\ a_5 = \boldsymbol{A}(x_0,y_{-1}) \\ a_6 = \boldsymbol{A}(x_1,y_1) \end{cases}. \tag{1}$$

As a consequence, the estimates of x and y are obtained in closed-form (see Appendix A for the mathematical derivation) from the estimated six samples of the ambiguity function, $a_1,\ldots,a_6$, namely [27]

$$\hat{x} = x_0 + \frac{-a(a_4-a_5)+b(a_2-a_3)}{2a^2-2bc} \tag{2}$$

and

$$\hat{y} = y_0 + \frac{-a(a_2-a_3)+c(a_4-a_5)}{2a^2-2bc}, \tag{3}$$

with $a = a_6+a_1-a_2-a_4$, $b = a_4+a_5-2a_1$, and $c = a_2+a_3-2a_1$. It is worth to underline that in (1), without loss of generality, the cross-correlation in (x_1,y_1) is assumed as the sixth point of the interpolating function. However, in general, as suggested in [27] a reasonable operating strategy to choose the sixth point among the four possible choices (x_1,y_1), (x_{-1},y_{-1}), (x_{-1},y_1), and (x_1,y_{-1}), consists of selecting that which has the maximum cross-correlation amplitude and then to utilize the associated equation. Therefore, from the formal viewpoint of the equations' system, the sixth equation based on the point (x_1,y_1) should be exchanged with the "best" one and the new solution should be accordingly derived. Nevertheless, the solution derived herein is still valid by rotating the domain (as well as the whole ambiguity function neighborhood) of 90°, 180°, and 270° in order to move the maximum value into the point (x_1,y_1) again and then exploiting (2)-(5). Another possibility could be to use all of them, hence solving an over-determined system of 9 equations with 6 unknowns by a pseudo-inverse matrix-based solution. However, as shown in [27] this strategy shows some losses in the estimation of the paraboloid peak, because it can be quite difficult to effectively exploit further correlation estimates which are far from its maximum, where the experienced signal strength is lower.

B. 1D Parabolic Interpolation of the 2D Ambiguity Function

In addition to the paraboloid interpolation described in the previous subsection, an alternative way to properly identify the true maximum position of a 2D ambiguity function could consist in applying two independent procedures that perform the 1D parabolic interpolation of the ambiguity cuts in the two competing directions. Therefore, following the leads of [28] and the procedure provided in [27], the estimation of the two parameters of the ambiguity function, viz. x and y, are again derived in closed-form from the estimated five samples $a_1,\ldots,a_5$, described in Subsection II-A, i.e.,

$$\hat{x} = x_0 - \frac{1}{2}\frac{a_2-a_3}{a_2+a_3-2a_1} \tag{4}$$

and

$$\hat{y} = y_0 - \frac{1}{2}\frac{a_4-a_5}{a_4+a_5-2a_1}. \tag{5}$$

Note that, in this case the additional information embedded in the sample a_6 is discarded.

C. Proposed Coregistration Algorithm

The proposed sub-pixel SAR images coregistration algorithm based on 2D parabolic interpolation of the 2D cross-correlation is shown in Figure 1. As depicted in the figure, it comprises some few steps that clearly emphasized the low computational complexity of the procedure. As a coregistration algorithm, it starts with the availability of two different SAR images of the same scene, possibly acquired at different time instants and/or at the same time but with a slightly different sensor position. The two images are typically referred to as master, $\boldsymbol{I}_m$, and slave, $\boldsymbol{I}_s$, and the algorithm is aimed at aligning the latter so as each pixel in it contained shares the same position within the former. The first step of the proposed procedure is the computation of the 2D spatial cross-correlation between $\boldsymbol{I}_m$ and $\boldsymbol{I}_s$. Formally, the 2D cross-correlation between the matrices $\boldsymbol{I}_m \in \mathbb{C}^{K\times N}$ and $\boldsymbol{I}_s \in \mathbb{C}^{K\times N}$, is a matrix $\boldsymbol{C}_{m,s} \in \mathbb{C}^{2K-1\times 2N-1}$, whose (k,n)-th element is given by [29]

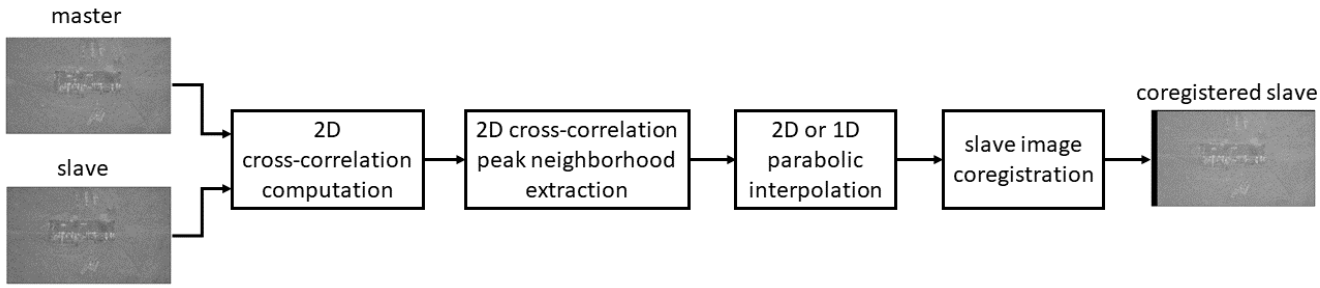

Figure 1. Block scheme of proposed sub-pixel SAR images coregistration algorithm.

$$\boldsymbol{C}_{m,s}(k,n) = \sum_{k=0}^{K-1}\sum_{n=0}^{N-1} \boldsymbol{I}_m(k,n)\boldsymbol{I}_s^*(k-h,n-p), \quad \begin{matrix} -K+1 \leq h \leq K-1, \\ -N+1 \leq p \leq N-1, \end{matrix} \tag{6}$$

where h and p represent the spatial shifts over range and azimuth directions, respectively. It is now worth to recall that (6) becomes the 2D auto-correlation when computed using the same image as master and slave.

After the 2D cross-correlation evaluation, the next step is the identification of the peak of the cross-correlation modulus (say (h_0, p_0)), representing the coarse shift estimate, and the consequent extraction of the sub-matrix containing the 3×3 neighborhood centered on it[1]. Since, the auto-correlation peak is at the center, namely in the position given by the spatial shifts $h = 0$ and $p = 0$, it follows that the position of the cross-correlation matrix directly give the displacement values in range and azimuth for the two considered master and slave images. Let now indicate with $\boldsymbol{C}_N \in \mathbb{C}^{3\times3}$, the matrix containing the extracted peak's neighborhood, (2)-(3) is applied to $a_1 = |\boldsymbol{C}_N(h_0, p_0)|$, $a_2 = |\boldsymbol{C}_N(h_0+1, p_0)|$, $a_3 = |\boldsymbol{C}_N(h_0-1, p_0)|$, $a_4 = |\boldsymbol{C}_N(h_0, p_0+1)|$, $a_5 = |\boldsymbol{C}_N(h_0, p_0-1)|$, and $a_6 = |\boldsymbol{C}_N(h_0+1, p_0+1)|$. The application of the latter operation provides an estimate of the paraboloid vertex, say $(\hat{h}, \hat{p})$, with an intrinsic sub-pixel accuracy, exploited then at the final coregistration step to obtain the properly translate resulting image, say $\boldsymbol{I}_c \in \mathbb{C}^{K\times N}$. Alternatively, to utilize the 1D parabolic interpolation strategy (this alternative of the algorithm is referred in the following as 1D parabolic based (1D-PB)) of Subsection II-B, (4)-(5) are applied to $a_1 = |\boldsymbol{C}_N(h_0, p_0)|$, $a_2 = |\boldsymbol{C}_N(h_0+1, p_0)|$, $a_3 = |\boldsymbol{C}_N(h_0-1, p_0)|$, $a_4 = |\boldsymbol{C}_N(h_0, p_0+1)|$, and $a_5 = |\boldsymbol{C}_N(h_0, p_0-1)|$.

Before concluding this subsection, Algorithm 1 summarizes the main steps of the proposed sub-pixel SAR image coregistration procedure.

[1]It is worth observing that the proposed method does not require knowledge of the overall cross-correlation; therefore, to properly manage the trade-off between the estimation accuracy of the cross-correlation peak and the computational burden, a patch from the quoted couple of images could be extracted as starting point for cross-correlation evaluation.

Algorithm 1 Sub-pixel SAR Image Coregistration Algorithm based on Parabolic Interpolation

Input: Master SAR image $\boldsymbol{I}_m \in \mathbb{C}^{K\times N}$, and slave SAR image $\boldsymbol{I}_s \in \mathbb{C}^{K\times N}$;
Output: Coregistered slave SAR image $\boldsymbol{I}_c \in \mathbb{C}^{K\times N}$;

1: 2D cross-correlation computation $\boldsymbol{C}_{m,s}$ between images $\boldsymbol{I}_m$ and $\boldsymbol{I}_s$ through (6);
2: 2D cross-correlation peak identification, (h_0, p_0);
3: 2D cross-correlation peak neighborhood extraction, $\boldsymbol{C}_N \in \mathbb{C}^{3\times3}$;
4: Paraboloid vertex location estimation, $(\hat{h}, \hat{p})$, applying (2)-(3) (for 2D-PB) or (4)-(5) (for 1D-PB) to $|\boldsymbol{C}_N|$;
5: Translation of the slave image $\boldsymbol{I}_s$ by a quantity $(\hat{h}, \hat{p})$ to obtain that coregistered to master, i.e., $\boldsymbol{I}_c$.

III. Other Coregistration Algorithms

Starting from two images of the same scene $\boldsymbol{I}_m$ and $\boldsymbol{I}_s$, different techniques can be utilized to perform the registration (alignment) of the slave over the master. In this paper, the following algorithms are considered as competitors of the proposed technique:

- 2D cross-correlation peak (CCP) technique;
- phase correlation (PC) procedure [6];
- fast normalized cross-correlation algorithm (fast NCCA) [7], [8].

A. CCP technique

This technique simply consists in computing the 2D spatial cross-correlation between the two images $\boldsymbol{I}_m$ and $\boldsymbol{I}_s$ through (6). The peak of this new quantity represents the estimate of the shift between the quoted images toward their registration.

B. PC procedure

The PC procedure designed in [6] is based on the exploitation of some shift properties of the Fourier transform. Precisely, starting from the two SAR images to register, i.e., $\boldsymbol{I}_m$ and $\boldsymbol{I}_s$, they are first 2D Fourier transformed, and then they spectra are multiplied and normalized so as to compute their cross-power spectrum, namely

$$\frac{\mathcal{F}(\boldsymbol{I}_m)\mathcal{F}(\boldsymbol{I}_s)^*}{|\mathcal{F}(\boldsymbol{I}_m)\mathcal{F}(\boldsymbol{I}_s)^*|}. \tag{7}$$

Since, the phase difference between the two original images offset by a quantity (h,p) is equal to the phase of their cross-power spectrum, the latter equation is equal to $e^{2\pi j(hk+pn)}$. Consequently, its inverse Fourier transform is characterized by a peak at the position (h,p), that is detected to perform the desired coregistration. Note that the PC is procedure gives the same results as the CCP which is only computed in an efficient manner thanks to fast Fourier transform (FFT) implementation. For this reason in the analysis section, we will refer only to the CCP technique.

C. Fast NCCA algorithm

The Fast NCCA algorithm proposed in [7], [8] consists in a nonlinear optimization problem that maximizes the coherent cross-correlation of the two images. Precisely, starting from $\boldsymbol{I}_m$ and $\boldsymbol{I}_s$, a first consists in a coarse registration of the two images. Once the coarsely registered slave image, $\boldsymbol{I}_{s0}$ say, is obtained, a fine registration is applied. The latter consists in searching for an optimal shifts h and p through the maximization of the coherent cross-correlation between $\boldsymbol{I}_m$ and $\boldsymbol{I}_{s\Delta}$, with $\boldsymbol{I}_{s\Delta}$ the interpolated version of $\boldsymbol{I}_{s0}$ with displacements h and p.

The displacement (h,p) is found solving the following optimization problem, which is a sequential quadratic programming (SQP) [30],

$$\begin{cases} (h,p) = \arg\max\limits_{(h,p)} |b_0 + b_1 h + b_2 p + b_3 hp| / \sqrt{c_0 c_1} \\ \text{s.t. } 0 \le h \le 1,\ 0 \le p \le 1 \end{cases}, \tag{8}$$

with

$$\begin{aligned} c_1 &= q_0 + q_1 h^2 + q_2 p^2 + q_3 h^2 p^2 + q_4 h + q_5 p \\ &\quad + q_6 h^2 p + q_7 h p^2 + q_8 hp, \end{aligned}$$

$$b_v = \sum_{k=0}^{K-1}\sum_{n=0}^{N-1} \boldsymbol{I}_m(k,n)\boldsymbol{Q}_v^*(k,n),\ v = 0,\dots,3,$$

$$q_v = \sum_{k=0}^{K-1}\sum_{n=0}^{N-1} \boldsymbol{Q}_v(k,n)\boldsymbol{Q}_v^*(k,n),\ v = 0,\dots,3,$$

$$q_v = \sum_{k=0}^{K-1}\sum_{n=0}^{N-1} \left(\boldsymbol{Q}_0(k,n)\boldsymbol{Q}_{v-3}^*(k,n) + \boldsymbol{Q}_0^*(k,n)\boldsymbol{Q}_{v-3}(k,n)\right), \quad v = 4,5,$$

$$q_6 = \sum_{k=0}^{K-1}\sum_{n=0}^{N-1} \left(\boldsymbol{Q}_1(k,n)\boldsymbol{Q}_3^*(k,n) + \boldsymbol{Q}_1^*(k,n)\boldsymbol{Q}_3(k,n)\right),$$

$$q_7 = \sum_{k=0}^{K-1}\sum_{n=0}^{N-1} \left(\boldsymbol{Q}_2(k,n)\boldsymbol{Q}_3^*(k,n) + \boldsymbol{Q}_2^*(k,n)\boldsymbol{Q}_3(k,n)\right),$$

$$\begin{aligned} q_8 = \sum_{k=0}^{K-1}\sum_{n=0}^{N-1} \Big(&\boldsymbol{Q}_0(k,n)\boldsymbol{Q}_3^*(k,n) + \boldsymbol{Q}_0^*(k,n)\boldsymbol{Q}_3(k,n) \\ &+ \boldsymbol{Q}_1(k,n)\boldsymbol{Q}_2^*(k,n) + \boldsymbol{Q}_1^*(k,n)\boldsymbol{Q}_2(k,n)\Big), \end{aligned}$$

$$c_0 = \sum_{k=0}^{K-1}\sum_{n=0}^{N-1} |\boldsymbol{I}_m(k,n)|^2.$$

Moreover, the matrices $\boldsymbol{Q}_v$, $v = 0,\dots,3$ are defined as $\boldsymbol{Q}_0 = \boldsymbol{I}_{s0}$, $\boldsymbol{Q}_1 = \boldsymbol{I}_{s0} * \boldsymbol{u}^T$, $\boldsymbol{Q}_2 = \boldsymbol{I}_{s0} * \boldsymbol{u}$, and $\boldsymbol{Q}_3 = \boldsymbol{I}_{s0} * [\boldsymbol{u}^T, \boldsymbol{v}^T]^T$, with $\boldsymbol{u} = [1,-1]^T$ and $\boldsymbol{v} = [-1,1]^T$.

IV. Performance Assessment

In this section, the capabilities of the proposed method in terms of sub-pixels image coregistration are tested over the Ku-band (16.74 GHz) spotlight UAV SAR images collected by a Sandia National Laboratory test platform[2] on 14 February 2006. The collection consists of two flights called "am" (for the morning flight) and "pm" (for the afternoon flight). The image (1754×3000 pixels), whose one-look spatial resolution is 0.120009 m in azimuth and 0.119972 m in range, represents a scene collected near Albuquerque, New Mexico; the corresponding optical image drawn from Google Earth© is shown in Figure 2.

Figure 2. Optical image of the observed scene (drawn from Google Earth©).

A. Tests on Single-Look Images

The analysis herein described is conducted on the Sandia single-look UAV SAR image "am/p07_003". Precisely, in order to have knowledge of the true image displacements among the couple of images, the slave is generated from the master by means of a rigid translation of it of a number of pixels equal to 58.5 pixels in the azimuth direction and 18.4 pixels in range direction[3]. The effect of the latter can be easily observed in Figure 3, where the relative displacements are clearly evident. Then, a sub-area (also referred to as image patch) of size 400×1300 pixels at the center of the two images is extracted

[2]Data can be downloaded at https://sandia.gov/radar/complex_data/.

[3]Note that, since the considered shift is equal to a non-integer number of pixels, the translated image is also re-sampled with a cubic interpolation.

to compute the 2D cross-correlation; this choice is done to manage the trade-off between estimation accuracy of the cross-correlation peak and the overall computational burden. Figure 4 depicts the isolevel curves of both the 2D auto-correlation of the master image and the 2D cross-correlation computed between the master and slave. As expected the auto-correlation presents its peak value at the image center, i.e., when the displacement in both range and azimuth directions is null. Conversely, the cross-correlation image shows a main peak at a position representing the displacement needed to realign the master and slave images.

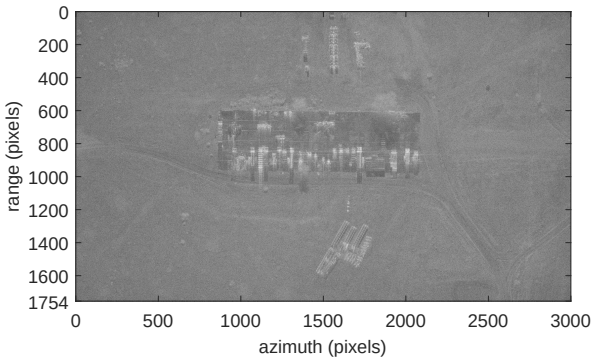

(a) master

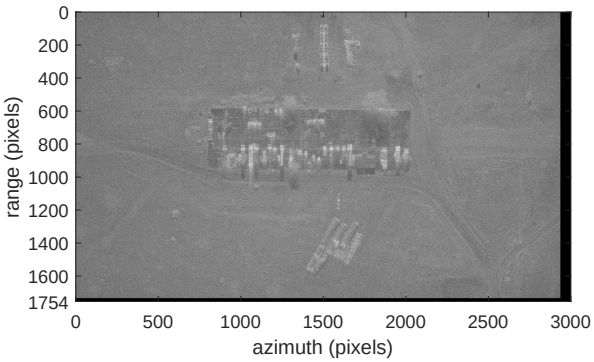

(b) slave

Figure 3. Master and slave images (modulus expressed in dB). Slave image obtained shifting the master image (reference image am/p07_003) of 58.5 and 18.4 pixels in azimuth and range directions, respectively.

The proposed PB algorithm starts from the extraction of the neighborhood of size 3×3 centered in the peak of the 2D cross-correlation, as illustrated in Figure 5(a). It is evident that the center value can be adjusted/refined through the proposed algorithm to find the best peak value obtained as the paraboloid vertex. This latter (red circle) is clearly shown in Figure 5(b) where the true displacement point is also indicated (blue square). From the inspection of the figure it is evident the capabilities of the PB algorithm to properly estimate the position of the true cross-correlation peak with a sub-pixels resolution.

In Figure 6 the two coregistered images obtained utilized the displacement given by the paraboloid peak, i.e., the results

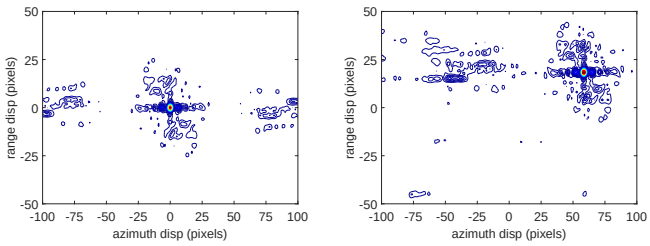

(a) auto-correlation (b) cross-correlation

Figure 4. Isolevel curves of the auto- and cross-correlations of master and slave images. Slave image obtained shifting the master image (reference image am/p07_003) of 58.5 and 18.4 pixels in azimuth and range directions, respectively.

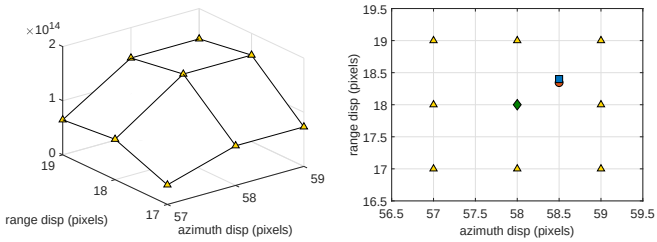

(a) cross-correlation (b) grid of points

Figure 5. Cross-correlations values (yellow triangles) around peak (green diamond) and considered grid of points together with estimated coordinates with the 2D-PB of paraboloid vertex (red circle). Slave image obtained shifting the master image (reference image am/p07_003) of 58.5 and 18.4 pixels in azimuth and range directions (true displacement represented by the blue square), respectively.

of the 2D-PB and CCP (see Subsection III-A) methods are shown. Even if it is not easy to appreciate by a visual inspection the differences between these two results, analyzing the values reported in Table I, it is evident the increment in the estimation accuracy of the true displacement achievable with the 2D-PB technique. To further emphasize the benefits of the proposed algorithm, Table I reports also the estimated displacements of the 1D-PB procedure (see Subsection II-B) and the fast NCCA (see Subsection III-C) [7], [8]. From the table, the improvement in term of sub-pixel shift estimation is evident. Moreover, the grand advantage of the proposed algorithm derives from the fact that the fine estimation of the displacement with the proposed PB procedure is given in closed-form, both for the 2D and 1D alternatives, and therefore characterized by a very low computational complexity. In fact, this latter is only ruled by the calculus of the cross-correlation peak. This claim is confirmed by the results reported in Figure 7, where the computational time is plotted versus the size of the patch extracted from the two images to compute the cross-correlation both for the entire algorithm and the only computation of the paraboloid peak. As expected the overall computation time, evaluated for a medium/low performing general purpose processor (see the figure caption for details), grows as the patch size increases, while it remains under 10 s even for a patch of 400×400 pixels wide. As to the paraboloid peak, it is always evaluated in time less than 0.1 s. So it

could be concluded that, if the cross-correlation is efficiently computed for instance applying the method of [6], the overall computational burden can be sufficiently reduced to allow the use of the proposed procedure also to real-time applications.

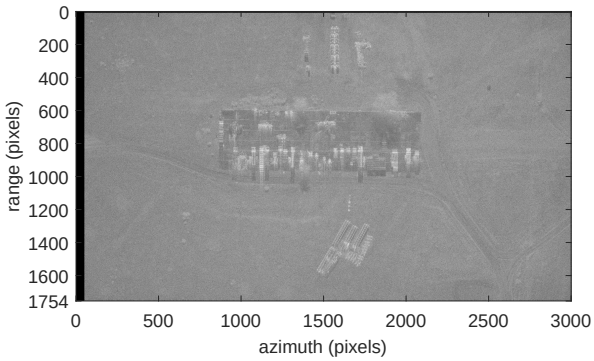

(a) 2D-PB

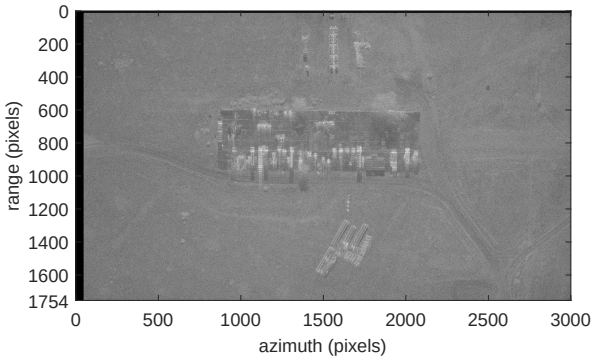

(b) CCP

Figure 6. Modulus of the coregistered SAR images (modulus expressed in dB). The original slave image was obtained shifting the master image (reference image am/p07_003) of 58.5 and 18.4 pixels in azimuth and range directions, respectively.

The second analysis is conducted again on the reference image "am/p07_003", with the slave generated now from the master by a rigid translation of 58 pixels in azimuth and 18 in range. Applying the same procedure as before, the isolevel curves of the 2D auto-correlation of the master and the 2D cross-correlation of master and slave images are computed and shown in Figure 8. As expected the auto-correlation presents its peak value at the image center, i.e., when the displacement in both range and azimuth directions is null. Conversely, the cross-correlation image shows a main peak at a position representing the displacement needed to realign the master and slave images.

As in first study case, in Figure 5(a) it is depicted the 3×3 neighborhood centered in the peak of the 2D cross-correlation whose points are then utilized to perform the paraboloid peak estimation. It is evident that now the center value is already correctly estimated by the cross-correlation maximum, since the displacement is an integer number. Therefore, the application of the proposed, as well as others, algorithm does not provide additional benefits. This can be better observed in Figure 9 where the neighborhood (yellow triangles) of

Table I. RANGE AND AZIMUTH ESTIMATED DISPLACEMENTS FOR SINGLE-LOOK IMAGES.

		range displacement	azimuth displacement
case 1	true value	18.4	58.5
	2D-PB	18.3446	58.4998
	1D-PB	18.3431	58.4985
	CCP	18	58
	fast NCCA	18.2814	58.9998
case 2	true value	18	58
	2D-PB	17.9998	58
	1D-PB	17.9998	58
	CCP	18	58
	fast NCCA	18.4999	58.0007

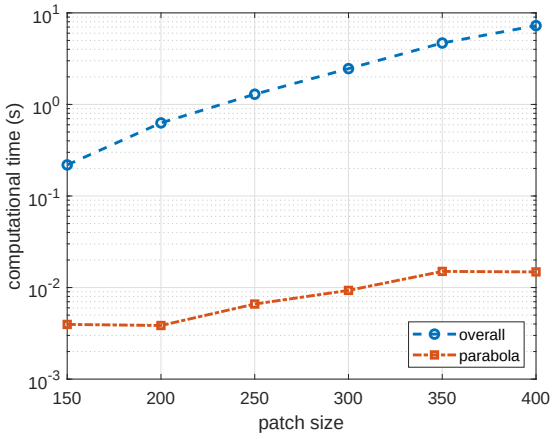

Figure 7. Computational time versus patch sizes. The curves refer to the time needed to execute the entire co-registration process, and that for only the computation of the paraboloid peak. This test is conducted on an Inter(R) Core(TM) i5 CPU at 2.2 GHz and 4.00 GB RAM.

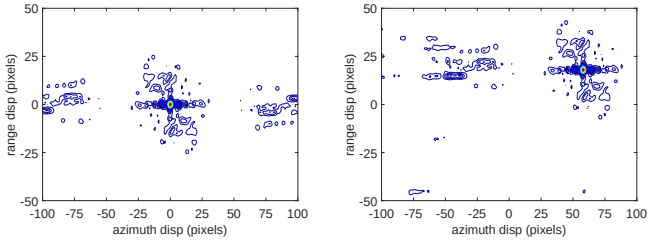

(a) auto-correlation (b) cross-correlation

Figure 8. Isolevel curves of the auto- and cross-correlations of master and slave images. Slave image obtained shifting the master image (reference image am/p07_003) of 58 and 18 pixels in azimuth and range directions, respectively.

the peak (green diamond) representing the coarse estimation, the true displacement (blue square) and the paraboloid vertex (red circle) are highlighted. The comparison with the other counterparts is reported in the second part of Table I.

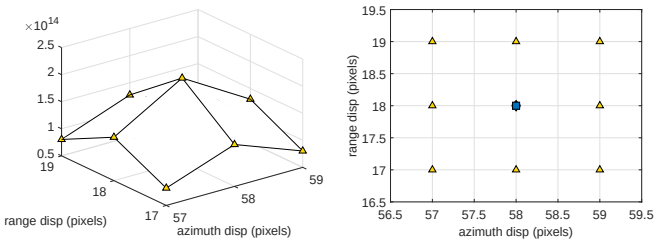

(a) cross-correlation (b) grid of points

Figure 9. Cross-correlations values (yellow triangles) around peak (green diamond) and considered grid of points together with estimated coordinates with the 2D-PB of paraboloid vertex (red circle). Slave image obtained shifting the master image (reference image am/p07_003) of 58 and 18 pixels in azimuth and range directions (true displacement represented by the blue square), respectively.

In addition to the estimated displacement values, a synthetic measure of the effectiveness of the applied coregistration techniques can be the coherence magnitude between the registered couple [31]. This latter is formally defined as

$$\rho = \left| \frac{\sum_{k=0}^{K-1}\sum_{n=0}^{N-1} \boldsymbol{I}_m(k,n)\boldsymbol{I}_c^*(k,n)}{\sqrt{\sum_{k=0}^{K-1}\sum_{n=0}^{N-1} |\boldsymbol{I}_m(k,n)|^2}\sqrt{\sum_{k=0}^{K-1}\sum_{n=0}^{N-1} |\boldsymbol{I}_c(k,n)|^2}} \right|, \quad (9)$$
$$-K+1 \leq h \leq K-1,$$
$$-N+1 \leq p \leq N-1.$$

The results of the coherence magnitude evaluation are given Table II for all the coregistered couples of images and for the two considered study cases. From the resulting values, the improvements obtained applying the registration procedure are evident, in fact the coherence magnitude between the two initial SAR images is low; conversely, the application of the above procedures produces a strong increment in the coherence between the quoted couple. Moreover, from the table, the gain obtained with the proposed technique can also be appreciated. As a matter of fact, the 2D- and 1D-PB always show the best performance for the considered tests.

Table II. COHERENCE MAGNITUDE BETWEEN THE STARTING AND COREGISTERED SAR IMAGES FOR SINGLE-LOOK IMAGES.

	non registered	2D-PB	1D-PB	CCP	NCCA
case 1	0.0013	0.9748	0.9748	0.8410	0.8829
case 2	0.0015	0.9996	0.9996	0.9996	0.8977

Now, to provide another quantitative analysis of the proposed algorithm also in comparison with its counterparts, herein we consider as figure of merit the absolute error of the displacement error in the azimuth and the range direction, respectively. Specifically, let us indicate with d_i the actual displacement in term of pixels in the direction i (that can be a azimuth or r range), and $\hat{d}_i$ the corresponding estimate, the displacement error is formally defined a

$$e_i = \hat{d}_i - d_i. \quad (10)$$

In Figure 10 the displacement error, computed through (10), is plotted versus d_i for the proposed coregistration technique, i.e., 2D- and 1D-PB, as well as the considered competitors, viz. CCP and NCCA. Subplots on the left refers to e_a for different azimuth displacements[4], viz., $d_a \in (0, 0.5)$, keeping fixed the range displacement d_r to the values 0, 0.25, and 0.5, respectively, for subplots (a), (c), and (e). Analogously, subplots on the right refers to e_r for different range displacements, viz., $d_r \in (0, 0.5)$, keeping fixed the azimuth displacement d_a to the values 0, 0.25, and 0.5, respectively, for subplots (b), (d), and (f).

The curves show that the proposed PB procedure has better performance than the considered counterparts, ensuring lower displacement error values for all the considered shifts. Interestingly, the PB shows displacements errors reaching zero at the extremes of the considered shifts interval, whereas, as expected the error of CCP grows as the sub-pixel displacement approaches the value 0.5.

To conclude this subsection, the displacement error of the proposed 2D-PB technique is computed considering image patches of different sizes extracted from the entire images; this is shown in Figure 11 for all the extracted patches, where subplots refer to patch sizes varying from 150×150 to 400×400 pixels. The aim of this test is to show the dependency of the PB algorithm on the quality of the cross-correlation peak neighborhood estimation. As a matter of fact, increasing the size of the considered image patch some increments in the performance are observed. However, when the cross-correlation is computed on a patch containing homogeneous areas with the absence of strong constant reflectors, such as buildings or man-made objects, the quality of the cross-correlation becomes poor, producing some performance losses during the 2D-PB evaluation process. Hence, if the extracted patches show a very poor coherence (e.g., on sea), the quality of the cross-correlation could be not sufficient enough to give insight about the displacement among the couple of images; this represent the main drawback that is common to all the cross-correlation based co-registration procedures. Nevertheless, the results of Figure 11 confirms the robustness of the 2D-PB with respect to the patch size.

B. *Tests on Multilook Images*

To have further insights about the usefulness of the proposed approach, herein the tests are conducted on SAR images just after the multilook process [1], [3]. Precisely, the Sandia

[4]Note that, this analysis is focused on evaluating the displacement estimation error in the case when it is of the order of the sub-pixel.

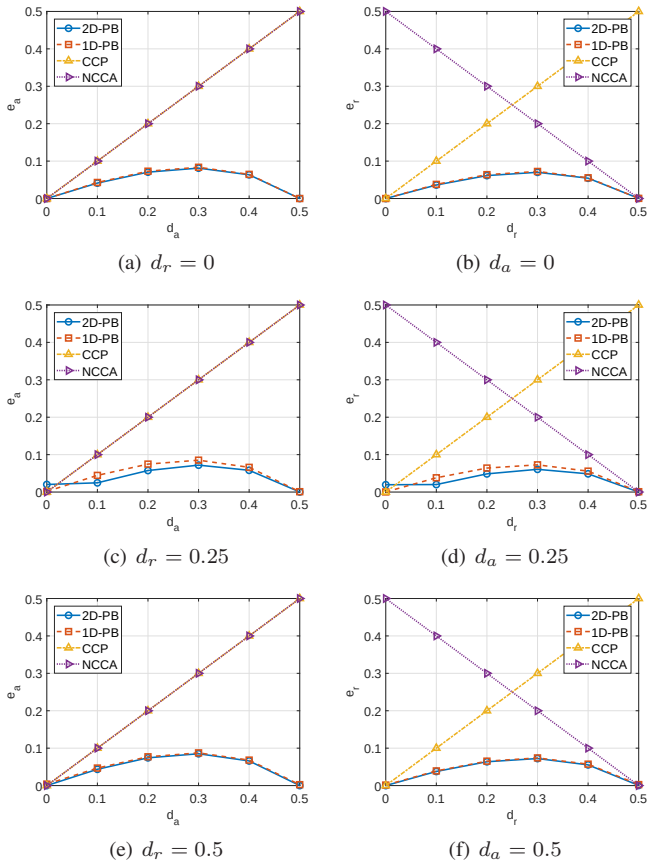

(a) $d_r = 0$ (b) $d_a = 0$

(c) $d_r = 0.25$ (d) $d_a = 0.25$

(e) $d_r = 0.5$ (f) $d_a = 0.5$

Figure 10. Displacement error versus true displacement. Subplots on the left refers to e_a for fixed range displacements d_r, whereas subplots on the right to e_r for fixed azimuth displacements d_a, namely, (a) $d_r = 0$, (b) $d_a = 0$, (c) $d_r = 0.25$, (d) $d_a = 0.25$, (e) $d_r = 0.5$, and (f) $d_a = 0.5$.

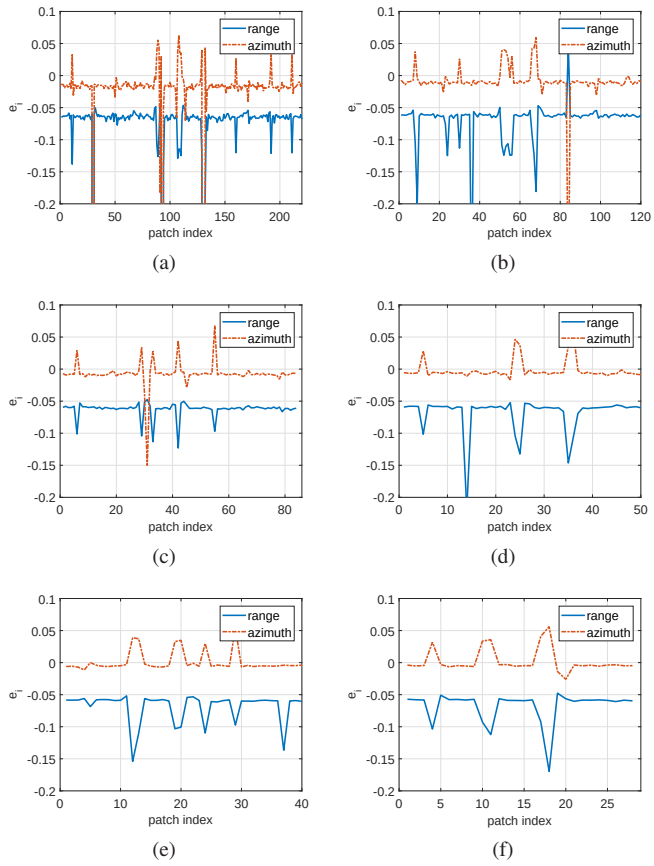

(a) (b)

(c) (d)

(e) (f)

Figure 11. Displacement error versus image patches. Subplots refer to different patch sizes, namely, (a) 150×150, (b) 200×200, (c) 250×250, (d) 300×300, (e) 350×350, (f) 400×400 pixels.

single-look UAV SAR image "am/p07_003" is used as master and the slave is again generated from it through a translation of 58.5 and 18.4 pixels in azimuth and range, respectively. Afterwards, the multilook process with a 5×5 sliding window is applied on the two images, whose modulus (expressed in dB values) is depicted in Figure 12. It is important to underline that the true displacement to compensate is equal to $(11.7, 3.68)$ in the multilook images even if the shift is applied before the multilook process.

As in the previous subsection, in Figure 13(a) the 3×3 neighborhood centered in the peak of the 2D cross-correlation is reported, moreover, Figure 13(b) shows this grid of points (yellow triangles) together with the estimated paraboloid vertex (red circle) with the 2D-PB algorithm and the true displacement point (blue square). In this case, to limit the computational burden, the 2D cross-correlation is computed from an image patch extracted from the master and slave of size 106×290 pixels. Again, just from a visual inspection of this figure the effectiveness of the proposed 2D-PB algorithm can be appreciated.

Table III summarizes the results of this study case on multi-look images comparing the obtained result with those of the considered counterparts. Again, the improvement in the estimation accuracy of the images displacement obtainable with the 2D-PB technique is clear. Nevertheless, in this specific scenario the best performances are achieved by the 1D-PB method which probably gather some advantages from the application of multi-look process with an integer shift of the original images.

Table III. RANGE AND AZIMUTH ESTIMATED DISPLACEMENTS FOR MULTI-LOOK IMAGES.

	range displacement	azimuth displacement
true value	3.68	11.7
2D-PB	3.716	11.7692
1D-PB	3.8388	11.9298
CCP	4	12
fast NCCA	4.9999	12.7989

As before, to give a further synthetic parameter testifying the effectiveness of the proposed method, the coherence magnitude

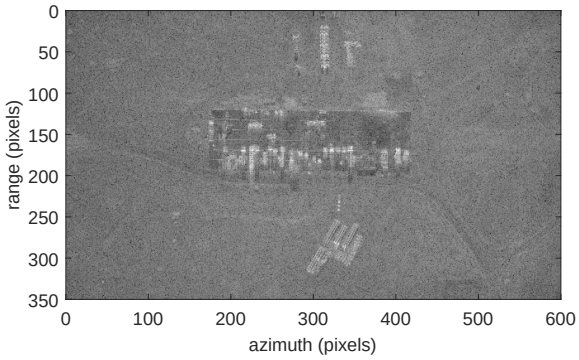

(a) master

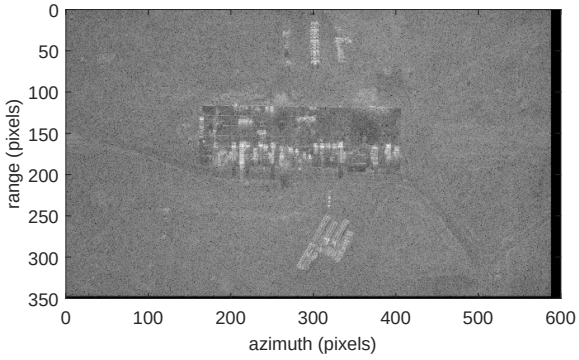

(b) slave

Figure 12. Master and slave images (modulus expressed in dB) after a 5×5 multilook process. Slave image obtained shifting the master image (reference image am/p07_003) of 58.5 and 18.4 pixels (i.e., 11.7 and 3.68 in the multilook images) in azimuth and range directions, respectively.

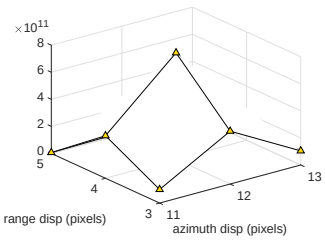

(a) cross-correlation

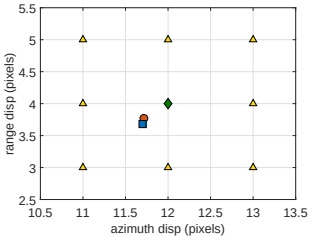

(b) grid of points

Figure 13. Cross-correlations values (yellow triangles) around peak (green diamond) and considered grid of points together with estimated coordinates with the 2D-PB of paraboloid vertex (red circle). Slave image obtained shifting the master image (reference image am/p07_003) of 58.5 and 18.4 pixels (i.e., 11.7 and 3.68 in the multi-look images) in azimuth and range directions (true displacement represented by the blue square), respectively.

is also computed for this test and the corresponding values are shown in Table IV. Again, the growth of coherence produced by the registration procedure is meaningful, moreover, the proposed PB method also gains over the considered counterparts. The main aim of this test after the multi-look process is to show the benefits provided by the proposed approach on low resolution SAR images with respect to the counterparts. As a matter of fact, though the initial considered shift is the same as considered in the single-look analysis, the 2D-PB share the best performance with a more significant gain over the other approaches, both in terms of estimated displacement and coherence, as shown in Tables III and IV.

Table IV. COHERENCE MAGNITUDE BETWEEN THE STARTING AND COREGISTERED SAR IMAGES FOR MULTI-LOOK IMAGES.

non registered	2D-PB	1D-PB	CCP	NCCA
0.0016	0.7197	0.6684	0.6268	0.0067

C. Tests on Scene Orientation

This section provides a study of the robustness of the proposed approach as a function of the orientation of the stronger reflecting object that are present within the illuminated scene with respect to the azimuth and range directions. Precisely, in the above considered images the majority of strong reflectors is vertically or horizontally aligned, i.e., in parallel to range and azimuth. In this section, before applying a translation, we rotate the starting image by an angle θ so as to modify the referred objects orientation. Precisely, the different orientation of the scene (together with that of the main structures contained in it) is simulated by means of a rotation of the images with a parametric angle (and consequently they are cut so as to obtain images as acquired by a different look angle). The considered tests are carried out again on the Sandia single-look UAV SAR image "am/p07_003", that is used as master. As already said, this image is rotated by θ and then the slave is generated from it through a translation in azimuth and range, respectively. In particular, three different tests (i.e., those corresponding to the cases analyzed in the previous subsections) are considered: a) the single-look case with a shift of 58.5 and 18.4 pixels in azimuth and range, b) the single-look case with a shift of 58 and 18 pixels in azimuth and range, and c) the multi-look case with a shift of 58.5 and 18.4 pixels in azimuth and range, respectively.

The considered figure of merit is still the coherence magnitude, ρ, defined in (9), that is computed for different values of the rotation angle, θ. The results of this test are depicted in Figure 14 for all the considered study cases. The curves highlight the benefits of applying the proposed 2D- and 1D-PB approaches, emphasizing also some gains of the former over the latter. Moreover, in the case of subplot b) the 2D-PB, 1D-PB, and CCP algorithms reach the same performances overcoming the NCCA.

D. Tests on Multi-Temporal Images

This last subsection is aimed at assessing the effectiveness of the proposed PB algorithm in coregister with a sub-pixel accuracy multi-temporal SAR images. To this end, the Sandia single-look UAV SAR image "am/p07_003" is used as master, whereas the image "pm/p07_003" assumes the role

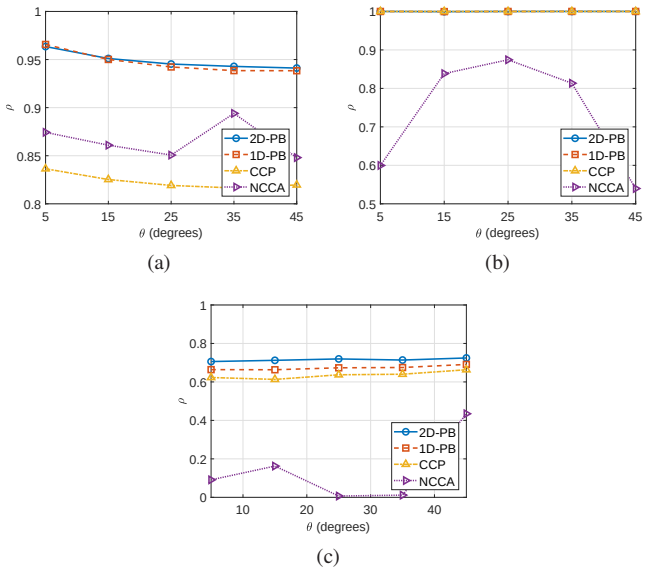

Figure 14. Coherence versus rotation angle. Subplots refer to (a) single-look and a shift of $(58.5, 18.4)$ pixels, (b) single-look and a shift of $(58, 18)$ pixels, and (c) multi-look and a shift of $(58.5, 18.4)$ pixels, respectively.

of slave. These couple of multi-temporal images is pictorially represented in Figure 15. From the figure observation it is easy to see that even these images represent the same scene, they show some differences in the reflected areas as well as a misalignment due to the different time instant of acquisition.

Figure 16 shows the cross-correlation values in the 3×3 neighborhood centered at it maximum value. Precisely, subplot (a) contains the cross-correlation values, whereas subplot (b) comprises their corresponding range-azimuth coordinates (yellow triangles) as well as the paraboloid vertex estimate (red circle). Since the exact true displacement cannot be available in such a situation, the effectiveness of the proposed approach can be understood only by a visual inspection of Figure 17 which is the slave image at the output of the proposed sub-pixels coregistration procedure. Nevertheless, as before, to have a quantitative measure of the improvement given by the coregistration techniques, the coherence magnitude computed between the registered couple through (9) comes in handy. As a matter of fact, the coherence magnitude values for the considered algorithms are 0.0896 for 2D-PB, 0.0881 for 1D-PB, 0.0831 for CCP, and 0.0752 for NCCA. Finally noting that the coherence between the master and slave images before the coregistration procedure is equal to 0.00064, it is evident which is the amount of improvement obtained with the proposed technique.

The last analysis herein performed shows the estimated displacement, i.e., $\hat{d}_i$, $i = r, a$, of the 2D-PB method evaluated extracting patches of different sizes from the quoted couple of images. The results of this test is reported in Figure 18, where again subplots refer to patch sizes varying from 150×150 to 400×400 pixels. By means of this test, the dependency of the 2D-PB algorithm on the quality of the cross-correlation peak neighborhood estimation is quantified. Differently form the

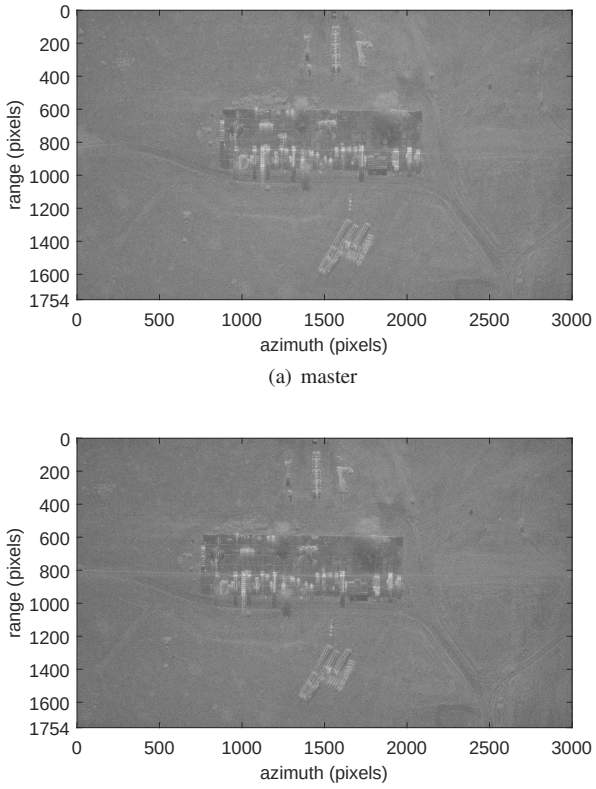

Figure 15. Master and slave images (modulus expressed in dB). The master is the reference image am/p07_003, whereas the slave the image pm/p07_003.

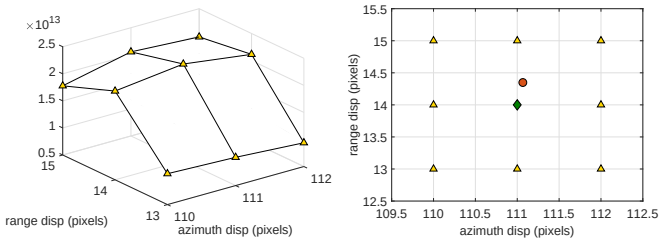

Figure 16. Cross-correlations values (yellow triangles) around peak (green diamond) and considered grid of points together with estimated coordinates with the 2D-PB of paraboloid vertex (red square). The master is the reference image am/p07_003, whereas the slave is the image pm/p07_003.

previous case, where the slave is simply a translated version of the master, now the two images are quite different each other, since they are acquired at different times. As a consequence, the graphs of the estimated shifts are more unstable than the previous case, thus strengthening the concept of appropriately selecting the patch to be processed.

V. Conclusions

In this paper a novel framework for SAR image registration with a sub-pixel accuracy is designed and analyzed. Precisely,

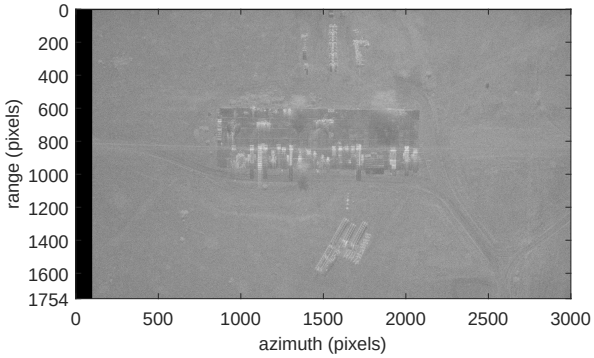

Figure 17. Modulus of the coregistered SAR image with the 2D-PB algorithm (modulus expressed in dB). The master is the reference image am/p07_003, whereas the slave is the image pm/p07_003.

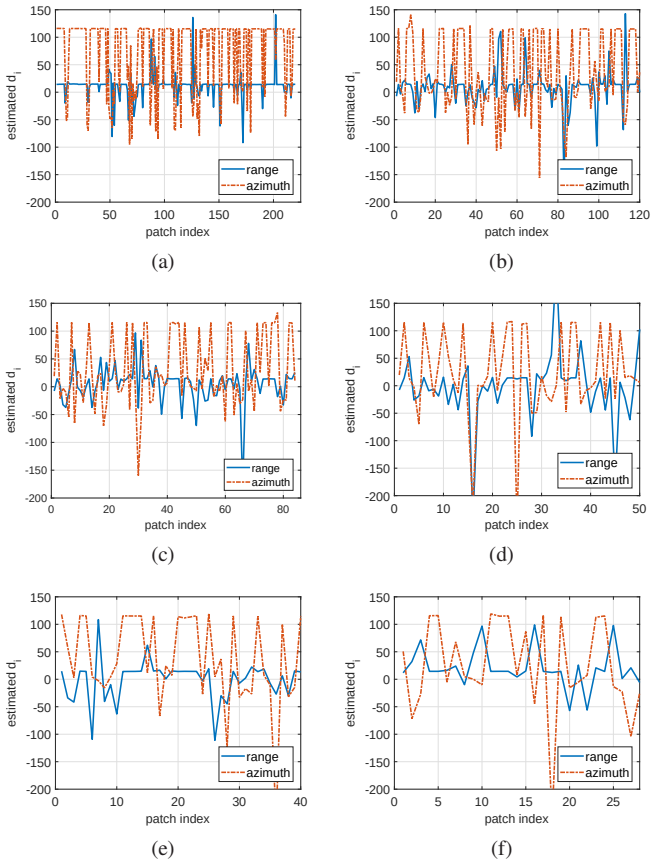

Figure 18. Estimated displacement with the 2D-PB method versus image patches for multi-temporal images. Subplots refer to different patch sizes, namely, (a) 150×150, (b) 200×200, (c) 250×250, (d) 300×300, (e) 350×350, (f) 400×400 pixels.

the devised algorithm exploits the 2D cross-correlation of the misaligned imagery to find a coarse estimate of the shift suffered by the slave image with respect to the master. The developed idea consists in performing a refinement of the estimated range and azimuth shifts through the application of a parabolic interpolation of the 2D cross-correlation. More precisely, once the cross-correlation peak has been identified, a neighborhood is extracted and the peak of the paraboloid interpolating those values is computed. In this work, two possible alternatives have been provided, the former that is the estimation of the 2D parabolid peak position from six values contained in the neighborhood, and the latter that consists in the estimation the two 1D parabola peak position in range and azimuth, respectively. Interestingly, both strategies allow to evaluate the paraboloid peak position with a closed-form expression, therefore with a very low computational burden, that is only ruled by the 2D cross-correlation calculus; this represents the grand advantage of the proposed strategy.

The analyses have been conducted on real recorded SAR data and have demonstrated the effectiveness of the proposed approach to provide a finer estimation of the images misaligned. In addition, improvements with respect to some counterparts have also been shown in terms of both absolute estimation error as well as coherence magnitude of among the quoted registered couple.

Possible future works might extend the proposed procedure to the complex field, exploiting also the phase information of the 2D cross-correlation of the two SAR images. Moreover, other interpolating functions (e.g., sinc-like) could be also introduced and analyzed. Finally, it could be of interest studying the improvements/losses experienced in the images coherence for different interpolating functions applied on the slave images, e.g., in different operating bands.

AKNOWLEDGMENT

The work of Dr Clemente was supported by the Engineering and Physical Sciences Research Council (EPSRC) Grant number EP/K014307/1 and the MOD University Defence Research Collaboration in Signal Processing.

The authors would like to thank Sandia National Laboratorie of National Technology and Engineering Solutions of Sandia, LLC., for providing the UAVSAR data. All data supporting this paper are available from https://sandia.gov/radar/complex_data/.

The authors would like to thank the Editor and the Referees for the interesting questions and comments that have helped to improve this paper.

APPENDIX

A. Derivation of the Peak Coordinates of the Interpolating Paraboloid from Six Available Points

To derive the paraboloid peak location described by (2)-(3), it is necessary to first solve the paraboloid equation, $\boldsymbol{A}(x,y) = \delta_1 x^2 + \delta_2 y^2 + \delta_3 xy + \delta_4 x + \delta_5 y + \delta_6$, passing for the six points given in (1), in the unknowns δ_i, $i = 1, \ldots, 6$, i.e.,

$$\begin{cases} a_1 = \delta_1 x_0^2 + \delta_2 y_0^2 + \delta_3 x_0 y_0 + \delta_4 x_0 + \delta_5 y_0 + \delta_6 \\ a_2 = \delta_1 x_1^2 + \delta_2 y_0^2 + \delta_3 x_1 y_0 + \delta_4 x_1 + \delta_5 y_0 + \delta_6 \\ a_3 = \delta_1 x_{-1}^2 + \delta_2 y_0^2 + \delta_3 x_{-1} y_0 + \delta_4 x_{-1} + \delta_5 y_0 + \delta_6 \\ a_4 = \delta_1 x_0^2 + \delta_2 y_1^2 + \delta_3 x_0 y_1 + \delta_4 x_0 + \delta_5 y_1 + \delta_6 \\ a_5 = \delta_1 x_0^2 + \delta_2 y_{-1}^2 + \delta_3 x_0 y_{-1} + \delta_4 x_0 + \delta_5 y_{-1} + \delta_6 \\ a_6 = \delta_1 x_1^2 + \delta_2 y_1^2 + \delta_3 x_1 y_1 + \delta_4 x_1 + \delta_5 y_1 + \delta_6 \end{cases}. \tag{11}$$

The latter can be rewritten in a compact matrix form as

$$\begin{pmatrix} a_1 \\ a_2 \\ a_3 \\ a_4 \\ a_5 \\ a_6 \end{pmatrix} = \begin{pmatrix} x_0^2 & y_0^2 & x_0 y_0 & x_0 & y_0 & 1 \\ x_1^2 & y_0^2 & x_1 y_0 & x_1 & y_0 & 1 \\ x_{-1}^2 & y_0^2 & x_{-1} y_0 & x_{-1} & y_0 & 1 \\ x_0^2 & y_1^2 & x_0 y_1 & x_0 & y_1 & 1 \\ x_0^2 & y_{-1}^2 & x_0 y_{-1} & x_0 & y_{-1} & 1 \\ x_1^2 & y_1^2 & x_1 y_1 & x_1 & y_1 & 1 \end{pmatrix} \begin{pmatrix} \delta_1 \\ \delta_2 \\ \delta_3 \\ \delta_4 \\ \delta_5 \\ \delta_6 \end{pmatrix}. \tag{12}$$

The above linear system is solved with inverse matrix computation, and the unknown coefficients δ_i, $i = 1, \ldots, 6$, are found. The paraboloid maximum is derived setting its gradient with respect to x and y equal to 0, namely

$$\frac{\partial \left(\delta_1 x^2 + \delta_2 y^2 + \delta_3 xy + \delta_4 x + \delta_5 y + \delta_6\right)}{\partial x} = 2\delta_1 x + \delta_3 y + \delta_4 = 0 \tag{13}$$

and

$$\frac{\partial \left(\delta_1 x^2 + \delta_2 y^2 + \delta_3 xy + \delta_4 x + \delta_5 y + \delta_6\right)}{\partial y} = 2\delta_2 y + \delta_3 x + \delta_5 = 0. \tag{14}$$

The peak coordinates is therefore the solution to the following linear system of 2 equations in 2 unknowns

$$\begin{cases} 2\delta_1 x + \delta_3 y + \delta_4 = 0 \\ 2\delta_2 y + \delta_3 x + \delta_5 = 0. \end{cases} \tag{15}$$

Hence,

$$x = \frac{2\delta_2 \delta_4 - \delta_3 \delta_5}{\delta_3^2 - 4\delta_1 \delta_2} \tag{16}$$

and

$$y = \frac{2\delta_1 \delta_5 - \delta_3 \delta_4}{\delta_3^2 - 4\delta_1 \delta_2}. \tag{17}$$

REFERENCES

[1] C. Olmsted, "Alaska SAR Facility Scientific SAR User's Guide," *Alaska SAR Facility Tech Rep ASF-SD-003*, 1993.

[2] M. A. Richards, *Fundamentals of Radar Signal Processing*, Tata McGraw-Hill Education, 2005.

[3] A. Moreira, P. Prats-Iraola, M. Younis, G. Krieger, I. Hajnsek, and K. P. Papathanassiou, "A Tutorial on Synthetic Aperture Radar," *IEEE Geoscience and Remote Sensing Magazine*, vol. 1, no. 1, pp. 6–43, 2013.

[4] Y. Wang, Q. Yu, and W. Yu, "An Improved Normalized Cross Correlation Algorithm for SAR Image Registration," in *2012 IEEE International Geoscience and Remote Sensing Symposium*. IEEE, 2012, pp. 2086–2089.

[5] Z. Zhang, H. Liu, L. Zhang, S. Wang, Z. Li, and J. Wu, "A Large Width SAR Image Registration Method Based on the Complex Correlation Function," in *2016 IEEE International Geoscience and Remote Sensing Symposium (IGARSS)*. IEEE, 2016, pp. 6476–6479.

[6] E. H. Peterson, G. Fotopoulos, A. Schmitt, R. E. Zee, and A. Roth, "Registration of Multi-Frequency SAR Imagery using Phase Correlation Methods," in *2011 IEEE International Geoscience and Remote Sensing Symposium*. IEEE, 2011, pp. 3708–3711.

[7] D. Li and Y. Zhang, "A Fast Offset Estimation Approach for InSAR Image Subpixel Registration," *IEEE Geoscience and Remote Sensing Letters*, vol. 9, no. 2, pp. 267–271, 2011.

[8] D. Li and Y. Zhang, "A Fast Normalized Cross-Correlation Algorithm for InSAR Image Subpixel Registration," in *2011 3rd International Asia-Pacific Conference on Synthetic Aperture Radar (APSAR)*. IEEE, 2011, pp. 1–4.

[9] R. Scheiber and A. Moreira, "Coregistration of Interferometric SAR Images using Spectral Diversity," *IEEE Transactions on Geoscience and Remote Sensing*, vol. 38, no. 5, pp. 2179–2191, September 2000.

[10] M. Ceccarelli, M. di Bisceglie, C. Galdi, G. Giangregorio, and S. L. Ullo, "Image Registration using Non-Linear Diffusion," in *IGARSS 2008 - 2008 IEEE International Geoscience and Remote Sensing Symposium*, July 2008, vol. 5, pp. V – 220–V – 223.

[11] A. Borzí, M. di Bisceglie, C. Galdi, and G. Giangregorio, "Robust Registration of Satellite Images with Local Distortions," in *2009 IEEE International Geoscience and Remote Sensing Symposium*, July 2009, vol. 3, pp. III–251–III–254.

[12] E. Sansosti, P. Berardino, M. Manunta, F. Serafino, and G. Fornaro, "Geometrical SAR Image Registration," *IEEE Transactions on Geoscience and Remote Sensing*, vol. 44, no. 10, pp. 2861–2870, October 2006.

[13] W. Zou and L. Chen, "Determination of Optimum Tie Point Interval for SAR Image Coregistration by Decomposing Autocorrelation Coefficient," *IEEE Transactions on Geoscience and Remote Sensing*, vol. 57, no. 7, pp. 5067–5084, July 2019.

[14] Z. Ma, M. Jiang, Y. Zhao, R. Malhotra, and B. Yong, "Minimum Spanning Tree Co-registration Approach for Time-Series Sentinel-1 TOPS Data," *IEEE Journal of Selected Topics in Applied Earth Observations and Remote Sensing*, pp. 1–10, 2019.

[15] J. Wang, Y. Pi, and Z. Cao, "Level Set Method for SAR Image Coregistration," *IEEE Geoscience and Remote Sensing Letters*, vol. 5, no. 4, pp. 615–619, October 2008.

[16] H. Goncalves, L. Corte-Real, and J. A. Goncalves, "Automatic Image Registration Through Image Segmentation and SIFT," *IEEE Transactions on Geoscience and Remote Sensing*, vol. 49, no. 7, pp. 2589–2600, July 2011.

[17] L. Zeng, D. Zhou, J. Liang, and K. Zhang, "Polar Scale-Invariant Feature Transform for Synthetic Aperture Radar Image Registration," *IEEE Geoscience and Remote Sensing Letters*, vol. 14, no. 7, pp. 1101–1105, July 2017.

[18] S. Paul and U. C. Pati, "A Block-Based Multifeature Extraction Scheme for SAR Image Registration," *IEEE Geoscience and Remote Sensing Letters*, vol. 15, no. 9, pp. 1387–1391, September 2018.

[19] W. Ma, Y. Wu, S. Liu, Q. Su, and Y. Zhong, "Remote Sensing Image Registration Based on Phase Congruency Feature Detection and Spatial Constraint Matching," *IEEE Access*, vol. 6, pp. 77554–77567, 2018.

[20] G. Yao, X. Man, L. Zhang, K. Deng, H. Zhuang, and G. Zheng, "Registrating Oblique SAR Images Based on Complementary Integrated Filtering and Multilevel Matching," *IEEE Journal of Selected Topics in Applied Earth Observations and Remote Sensing*, pp. 1–13, 2019.

[21] Y. Zhang and T. Wu, "An SAR Image Registration Method Based on Pyramid Model," in *2016 CIE International Conference on Radar (RADAR)*, October 2016, pp. 1–5.

[22] Y. Xiangab, W. Kangab, F. Wanga, and H. Youab, "Automatic Coregistration for Multiview SAR Images in Urban Areas," *Interna-*

tional Archives of the Photogrammetry, Remote Sensing and Spatial Information Sciences, vol. 42, no. 2/W7, 2017.

[23] J. Yun-hui, "Optical/SAR Image Registration based on Cross-Correlation with Multi-Scale and Multi-Direction Gabor Characteristic Matrixes," 2013.

[24] Y. Ye, J. Shan, L. Bruzzone, and L. Shen, "Robust Registration of Multimodal Remote Sensing Images Based on Structural Similarity," *IEEE Transactions on Geoscience and Remote Sensing*, vol. 55, no. 5, pp. 2941–2958, May 2017.

[25] J. Fan, Y. Wu, M. Li, W. Liang, and Y. Cao, "SAR and Optical Image Registration Using Nonlinear Diffusion and Phase Congruency Structural Descriptor," *IEEE Transactions on Geoscience and Remote Sensing*, vol. 56, no. 9, pp. 5368–5379, September 2018.

[26] Y. Ye, L. Bruzzone, J. Shan, F. Bovolo, and Q. Zhu, "Fast and Robust Matching for Multimodal Remote Sensing Image Registration," *IEEE Transactions on Geoscience and Remote Sensing*, pp. 1–12, 2019.

[27] G. Giunta, "Fine Estimators of Two-Dimensional Parameters and Application to Spatial Shift Estimation," *IEEE Transactions on Signal Processing*, vol. 47, no. 12, pp. 3201–3207, 1999.

[28] G. Jacovitti and G. Scarano, "Discrete Time Techniques for Time Delay Estimation," *IEEE Transactions on Signal Processing*, vol. 41, no. 2, pp. 525–533, February 1993.

[29] R. C. Gonzalez and R. E. Woods, *Digital Image Processing*, Pearson/Prentice Hall, Upper Saddle River, NJ, 3rd edition, 2008.

[30] P. T. Boggs and J. W. Tolle, "Sequential Quadratic Programming," *Acta Numerica*, vol. 4, pp. 1–51, 1995.

[31] R. Touzi, A. Lopes, J. Bruniquel, and P. W. Vachon, "Coherence Estimation for SAR Imagery," *IEEE Transactions on Geoscience and Remote Sensing*, vol. 37, no. 1, pp. 135–149, January 1999.

Luca Pallotta (S'12-M'15-SM'18) received the Laurea Specialistica degree (cum laude) in telecommunication engineering in 2009 from the University of Sannio, Benevento, Italy, and the Ph.D. degree in electronic and telecommunication engineering in 2014 from the University of Naples Federico II, Naples, Italy. He is currently an Assistant Professor at University of Roma Tre, Italy. His research interest lies in the field of statistical signal processing, with emphasis on radar/SAR signal processing, radar targets classification, polarimetric radar/SAR. Dr. Pallotta won the Student Paper Competition at the IEEE Radar Conference 2013.

Gaetano Giunta (M'88-SM'12) received the Electronic Engineering degree from the University of Pisa, Italy, and the Ph.D. degree in Information and Communication Engineering from the University of Rome La Sapienza, Italy, in 1985 and 1990, respectively. He was also (since 1989) a Research Fellow of the Signal Processing Laboratory (LTS) at EPFL, Lausanne, Switzerland. In 1992, he became an Assistant Professor with the INFO-COM Department, University of Rome La Sapienza. From 2001 to 2005, he was with the Third University of Rome as an Associate Professor. Since 2005, he has been a Full Professor of Telecommunications with the same University. His research interests include signal processing for mobile communications, image communications and security. Prof. Giunta has been a member of the IEEE Societies of Communications, Signal Processing, and Vehicular Technology. He has also served as a reviewer for several IEEE transactions, IET (formerly IEE) proceedings, and EURASIP journals, and a TPC member for several international conferences and symposia in the same fields.

Carmine Clemente (S'09-M'13-SM'18) received the Laurea (cum laude) (B.Sc.) and (M.Sc.) Laurea Specialistica (cum laude) degrees in telecommunications engineering from Università degli Studi del Sannio, Benevento, Italy, in 2006 and 2009, respectively, and the Ph.D. degree in signal processing from the Department of Electronic and Electrical Engineering, University of Strathclyde, Glasgow, U.K. He is currently a Senior Lecturer with the Department of Electronic and Electrical Engineering, University of Strathclyde working on advanced Radar signal processing algorithms, micro-Doppler analysis, SAR image processing and advanced radar applications. Dr Clemente directs the Sensor Signal Processing & Security Laboratories at the University of Strathclyde, his group research interests include micro-Doppler signature analysis and extraction, waveform design, passive and multi-static radars, automatic target recognition, electronic surveillance, space situation awareness, ballistic missile defence, automotive radars, applications of radars in Industry 4.0 and Agritech and statistical signal processing.